Arab J. Nucl. Sci. Appl., Vol. 58, 4, 61-74(2025)

ISSN 1110-0451

Arab Journal of Nuclear Sciences and Applications

Web site: ajnsa.journals.ekb.eg

(E S N S A)

Competitive Sorption Behavior of Some Metal Ions of Nuclear and Industrial Interest in Highly Acidic Solution Using Chitosan- Acrylic Acid Polymeric Resin Prepared by Gamma Radiation

Reham S. Hassan

Assistant professor of inorganic chemistry at the Analytical Chemistry and Control Department, Hot Laboratories Centre, Egyptian Atomic Energy Authority, Post Code 13759, Cairo, Egypt.

HIGHLIGHTS

1. A biodegradable chitosan–acrylic acid (CS-PAA) hydrogel was synthesized via gamma-induced graft polymerization using Co-60 at 5 kGy/h.
2. The CS-PAA hydrogel exhibited high removal efficiencies for metal ions at pH 4: Zr(IV): 92.4%, Gd(III): 84.9%, Sr(II): 62.8%
3. .The hydrogel adsorbent's maximum adsorption capacities for Sr (II), Gd (III), and Zr (IV) were 48.2, 57.6, and 66.7 mg/g, respectively
4. The material demonstrated good reusability, retaining significant adsorption capacity after four adsorption–desorption cycles.
5. Kinetic modeling indicated that the sorption process followed pseudo-second-order kinetics, suggesting a chemisorption-driven mechanism.

GRAPHICAL ABSTRACT

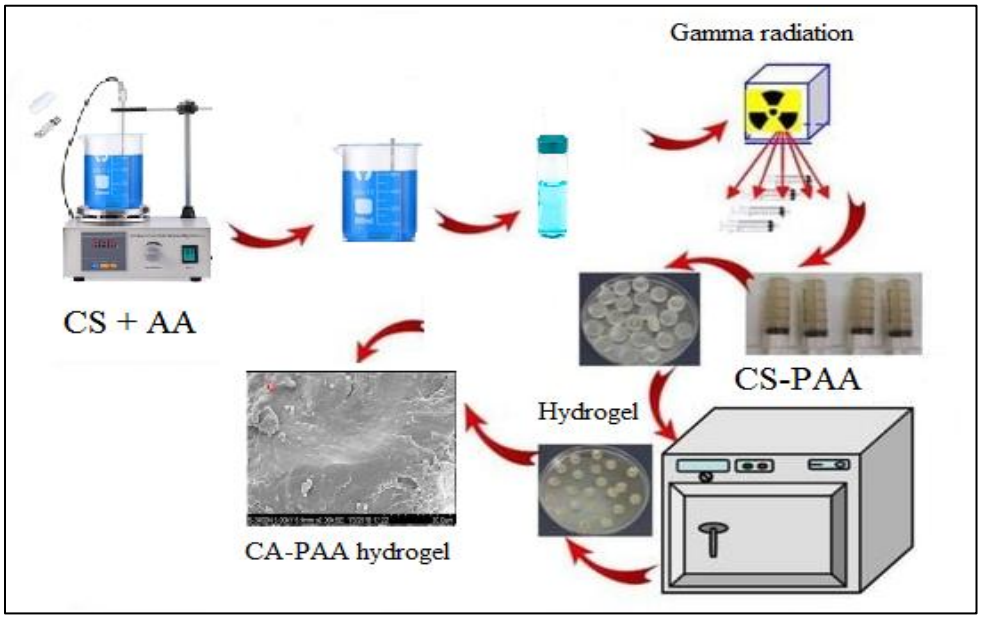

ARTICLE INFO

Article history:

Received: 21st July 2025

Accepted: 27th Aug. 2025

Available online: 20th Sept. 2025

Keywords:

Gamma radiation,
Grafting,
chitosan polyacrylic acid,
Sr (II),
Gd (III),
Zr (IV).

ABSTRACT

The current investigation is conducted to evaluate the sorption capability of an environmentally friendly adsorbent polymer chitosan acrylic acid (CS-PAA) towards some metal ions such as Sr (II), Gd(III) and Zr(IV). The polymer is prepared by grafting polymerization using gamma ray. It was exposed to 4.8 kGy/h of absorbed doses of Co-60 radioactive source for γ-radiation. Scanning electron microscopy (SEM), thermos-gravimetric analysis (TGA), and Fourier-transform infrared spectroscopy (FT-IR) were utilized to investigate the chemical structure and morphological characterizations of the hydrogel polymer. The FT-IR data demonstrated that grafting the acrylic acid onto the chitosan backbone was accomplished satisfactorily. While the SEM revealed a surface with a homogeneous and interconnected pore structure. The adsorption experiments demonstrated that, the polymer eliminated 92.4%, 84.9%, and 62.8% of Zr (IV), Gd (III) and Sr (II) ions, respectively at pH 4. The hydrogel adsorbent's maximum adsorption capacities for Sr (II), Gd (III), and Zr (IV) were 68.9, 74.2, and 80.4 mg/g, respectively. The utilized adsorbent could be regenerated for further usage and the regenerated adsorbent was still able to maintain adsorption capabilities that were nearly identical to the original after four adsorption-desorption cycles. The most appropriate fit to the kinetic data was pseudo second order (R^2 = 0.99 for Zr, 0.98 for Gd, and 0.97 for Sr), suggesting a mechanism driven by chemisorption. Equilibrium isotherm data were fitted and the Sips model best described the adsorption behavior across all metal ions (R^2 > 0.98), capturing both homogeneous and heterogeneous site interactions.

Corresponding author: dr.reham.eae.eg@gmail.com

DOI: 10.21608/ajnsa.2025.404696.1893

©Scientific Information, Documentation and Publishing Office (SIDPO)-EAEA

1. INTRODUCTION

The global movement toward sustainability, especially the utilization of natural resources, has generated a lot of interest in green materials for a variety of uses. Chitosan (CS), a natural polymer gained by de-acetylating, has become a potential cationic polysaccharide for biomaterials. Its antibacterial activity, wound-healing ability, biocompatibility, biodegradability, and non-toxicity are the reasons for this [1-3]. Due to the high concentration of active amino and hydroxyl groups, CS is a substance that may be altered and used in a variety of ways [5-6].

Copolymerization between chitosan and other polymers has been extensively studied [7] to address some of the drawbacks of (CS), such as its low mechanical strength, limited chain flexibility, low heat resistance, or low adsorbent selectivity. The two main copolymerization techniques are physical interactions between polymers in one or more phases [8] and, to a lesser extent, chemical changes like graft polymerization and cross-linking. Therefore, this Study will primarily focus on these two last procedures. To put it simply, a graft copolymer is composed of either a high weight macromolecular chain of one monomer, called the backbone polymer, with one or more branches, or grafts of different monomers or polymers (Fig. 2A) [9–11]. It has been shown that graft polymerization of acrylic acid to natural polymers improves water absorptivity, which raises chitosan's affinity for metal ion chelation [12-13]. The carboxylic groups of the acrylic monomer combine with the amino groups of chitosan to form a compound. A hydrogel is produced when the acrylic monomer polymerizes and the resultant polyacrylic acid chains interpenetrat the chitosan chains in an interpenetrating network. It has been demonstrated that ionizing radiations are easy and effective instruments for creating co- polymers, polymer blends, and nanocomposites [14-16]. Graft copolymer synthesis can be done in a variety of ways. Vinyl monomers are grafted onto the CS backbone to create the majority of copolymers [17].

However, the majority of biodegradable polymers, including polylactic acid, polycaprolactone, cellulose, and polyhydroxyalcanoates, lack vinyl groups [18]. Conversely, cross-linked polymers are those in which the chains of various polymers cross through physical interaction or chemical bonding between the polymers and monomers [19]. Graft polymerization and cross-linking allow for the addition of a broad range of functional groups to the CS chain, which opens up new applications in a number of sectors, including medical devices, water treatment, and metal adsorption. The elements Strontium, Gadolinium, and Zirconium each have distinct nuclear and industrial significance, which make them valuable in various applications. ^{90}Sr is of concern in nuclear waste management due to its mobility in the environment and potential uptake in bones (mimics calcium). While, Stable strontium is used in ceramics and glass, especially color cathode ray tubes (CRTs) and fireworks (for red color). It is also used in metal alloys and ferrite magnets [20-22].

Gadolinium has an exceptionally high neutron capture cross-section**,** particularly isotopes Gd-155 and Gd-157**.** It is widely used as a neutron absorber in nuclear reactor control rods and burnable poisons, which help control reactivity and improve fuel efficiency. Also used in nuclear shielding materials to protect against neutron radiation [23].

Because of their low neutron absorption cross-section, which makes them perfect for reactor conditions, zirconium alloys are essential to the nuclear industry. Outstanding resistance against corrosion at elevated temperatures. Its main application is as a material for cladding for light-water reactor (LWR) nuclear fuel rods. Utilized in radiation-exposed structural elements and nuclear reprocessing equipment as well [24–27].

The purpose of this research is to develop and figure out an environmentally friendly chitosan–acrylic acid (CS-PAA) hydrogel adsorbent**,** synthesized via gamma radiation-induced grafting, for the effective adsorption and recovery of Sr(II), Gd(III), and Zr(IV) ions from an aqueous solutions. The research seeks to investigate the structural, morphological, and thermal properties of the synthesized polymer and assess its adsorption performance, kinetics, isotherms, and reusability**,** with the goal of demonstrating its potential application in radioactive waste treatment and environmental remediation**.**

2. MATERIALS AND EXPERIMENTAL TECHNIQUES

2.1. Materials

Sigma Aldrich supplied the low molecular chitosan (CS), which has a degree of acetylation of 75–85% and a solubility viscosity of 20–200 Cp (1% solution in 1% acetic acid). Merck (Germany) was the provider of acrylic acid monomer (MW=72.06 g/mol). Fluka's HCl and/or NaOH were employed to modify the medium pH. In order to provide aqueous solutions for manufacturing, bi-distilled water was utilized.

2.2 Polymer preparation

10 g of chitosan (>75% de-acetylated) was decomposed in 100 mL of 1% (v/v) acetic acid under magnetic stirring during night at room temperature. . In a flask, add 23.98 mL acrylic acid to a volumetric flask and bring to 100 mL with DI water (final 4.0 M). Then, acrylic acid was added in 1:1 w/w monomer to polymer ratio with contentious steering to ensure complete mixing. After that, the solution was poured into glass vials at adjusted pH=4 and exposed to gamma radiation. Irradiation was carried out using a Co-60 gamma source at a dose rate of 4.8 ± 0.2 kGy/h (calibrated by Fricke dosimetry). Samples were irradiated to a total dose of 20 kGy at 25 ± 2 °C in a rotating sample holder (2 rpm) to ensure uniform exposure. Immediately after irradiation, hydrogels were removed from the vials and immersed in 0.1 M $NaHCO_3$ solution (3× gel volume) for 30 min under gentle agitation (100 rpm) to neutralize residual acid. Gels were then washed sequentially with DI water:EtOH (80:20 v/v) for 2 h and with deionized water and until neutral pH. Finally, the polymer hydrogel is oven-dried at 50 ^oC [28].

2.2.1 Characterization of natural chitosan (CS) and chitosan acrylic acid (CS-PAA)

SEM and Fourier Transform Infrared (FT-IR) were used to obtain chemical and physical parameters of natural CS and CS-PAA samples, as well as thermal analyses (TGA&DTA). Scanning Electron Microscopy, Jeol model JSM 5610 AL, Japan, was used to record the morphology of both natural CS and CS-PAA powder. A spectrometer model system 2000 FT-IR from Perkin Elmer Co., USA, was used to obtain the FT-IR spectra at wavelength of 400–4000 cm^{-1}, the spectrum was taken. The sample was thermally analysed using a Shimadzu DT-60 thermal analyzer from Japan, with a heating rate of 10^oC/min and nitrogen gas as a follow-up to avoid thermal oxidation.

2.2.2 Chemical stability at different pH

To describe the chemical stability of chitosan–poly (acrylic acid) (PAA) complexes through weight loss, 0.05 gm of polymer initial weight (*Wo)* is immersed at different buffered [29] pH solutions (1-12) individually for period time 1-24 hours. After that samples were washed, dried and weighted final weight (*Wt*), the weight loss percent (*W%*) was calculated using the equation:

$$W\% = Wo\text{-}Wt/WoX100 \quad \textbf{(1)}$$

2.2.3 Bach Investigation.

For evaluating the behavior of CS-PAA as adsorbent, batch adsorption measurements were carried out. Typically, to reach adsorption equilibrium, 0.2g of adsorbent was combined with 25 mL of the investigated ion Sr(II), Gd(III) and Zr(IV) solutions at different contact time, different pH range (1-12), different metal ion concentration (50-500 ppm) and different concentration of HCl acid (0.01, 0.05, 0.1, 0.2, 0.5 M). Samples were shaken in a thermostatic shaker for one hour at ambient temperature and 130 r/min. Following filtration, an ultraviolet spectrophotometer (A Perklin Elmer UV/Vis spectrometer Lambda 14) is used for experiments on liquid sample and absorbance is measured over the wavelength range of 200–900 nm. Arsenazo (III) is the complexing agents utilized in this investigation. Sr(II), Gd(III) and Zr(IV) have maximal absorption wavelengths between 650 nm, and 665 nm.

Kinetic and isotherm measurements were conducted for the investigated metal ions at acidic medium and room temperature (298 K).

The theoretical quantity adsorbed at equilibrium (q_e, mg/g), the adsorption percentage (R%), and the adsorbed quantity at any given time (q_t mg/g) were all calculated using the following formulas.

$$R\% = \left(\frac{C_0 - C_e}{C_0}\right) \times 100 \quad \textbf{(2)}$$

$$q_e = \frac{\left[\left(C_o - C_e\right)V\right]}{m} \quad \textbf{(3)}$$

$$q_t(mg/g) = \frac{C_o - C_t}{C_t} \times \frac{V}{m} \quad \textbf{(4)}$$

Where, m is the sorbent mass (g); V is the solution volume (L); and Co is the initial metal ion concentration and Ce is the metal ion concentrations at equilibrium (mg/L), respectively.

2.3. Models of Kinetic adsorption

2.3.1 Pseudo second ordered

The adsorption process is commonly described using the pseudo-second-order kinetic model (POS), especially in situations where chemisorption is the rate-limiting phase. This model relies on the idea that adsorption happens through valence forces, which are created when the adsorbent and adsorbate share or exchange electrons. Its non-linear form of the pseudo-second order (PSO) model is given by the following formula:

$$q_t = \frac{K_2 q_e^2 t}{1 + K_2 q_e t} \quad \textbf{(5)}$$

Where, K_2 (g/mg.min) is the rate constants of the PSO models, q_e and q_t (mg/g) are the quantity of metal ions sorbed at equilibrium and at time t respectively [30].

2.3.2 Elovich model

Chemisorption processes on heterogeneous surfaces are frequently described by the Elovich kinetic model. Because of the increased surface covering and activation energy for additional adsorption, it is assumed that the adsorption rate falls exponentially as the amount adsorbed increases. This model is particularly helpful in systems where the number of active sites increases exponentially with adsorption or where surface diffusion is the rate-limiting phase. Typically, the Elovich non-linear equation is written as follows:

$$q_t = \frac{\ln[\alpha\beta t]}{\beta} \qquad (6)$$

Where α is the initial adsorption rate (mg·(g·min)-1), qt is the adsorbed investigated metal ions ions (mg·g-1) at time t (min), and β is associated with the chemisorption activation energy (g·mg-1).

2.3.3 Intra particle diffusion

The intra-particle diffusion model, also called the Weber–Morris model, is used to determine if the diffusion of adsorbate molecules into the internal pores of the adsorbent particles is what is responsible for the rate-limiting phase of an adsorption process. The IPD model takes into account interior pore diffusion and is especially helpful for porous materials, in contrast to pseudo-second-order models that presume adsorption mostly takes place at the exterior surface. The non-linear equation is written as follows:

$$q_t = K_{diff} * t^{1/2} + C \qquad (7)$$

Where C is the boundary layer thickness value ($mg \cdot g^{-1}$) and k_{diff} is the intraparticle diffusion rate constant ($mg \cdot g^{-1}\ min^{1/2}$).

2.4. Isotherm adsorption models

Adsorption isotherm models describe how adsorbate molecules interact with adsorbent surfaces at constant temperature. These models are essential to understanding the capacity, mechanism, and the adsorbent's surface properties. Below is an overview of the four models commonly used.

2.4.1 Langmuir Isotherm Model.

Langmuir adopts the assumption that a monolayer will adsorb onto a surface that has a finite number of sites that are equal and energetically equivalent. Once a site is occupied, no further adsorption can occur at that site (monolayer coverage) and No interaction between adsorbed molecules [31].

$$q_e = \frac{q_m K_L C_e}{1 + K_L C_e} \qquad (8)$$

Where Ce is the residual adsorbate concentration at equilibrium (mg L^{-1}), K_L is the Langmuir equilibrium constant (L mg^{-1}), q_{max} is the maximum adsorption, and q_e is the amount of adsorbate adsorbed at equilibrium (mg g^{-1}).

2.4.2 Freundlich Isotherm Model

Freundlich assumes that the concentration of the adsorbate is correlated with the adsorption capacity when describing multilayer adsorption on heterogeneous surfaces. First to be occupied are the stronger binding sites. [32].

$$q_e = K_F C_e^{1/n} \qquad (9)$$

2.4.3 Temkin Isotherm Model

Temkin implies that binding energy is equally distributed up to a certain maximum binding energy and that the heat of adsorption reduces linearly with coverage, taking into account interactions between the adsorbent and the adsorbate.

$$q_e = B \ln(AC) \qquad (10)$$

Where b is the Temkin constant and B is a constant associated with the heat of adsorption = RT/b. Temkin isotherm constant (L/g) is (A).

2.4.4 Sips Isotherm Model (Langmuir–Freundlich Hybrid)

Sips model predicts adsorption on heterogeneous surfaces by combining the Langmuir and Freundlich models, particularly when the system behaves like Langmuir at high concentrations. At low concentrations, it operates similarly to the Freundlich model, whereas at large concentrations, it resembles the Langmuir model.

$$q_e = \frac{q_m (KC_e)^n}{1+(KC_e)^n} \quad (11)$$

$$q_e = \frac{K_s C_e^{Bs}}{1+a_s C_e^{Bs}} \quad (12)$$

2.5. Adsorption–Desorption Cycles for Sr(II) Gd(III) and Zr(IV)

First, 0.1 g of CS-PAA was combined with 0.05 L of 100 ppm of Sr(II) Gd(III) and Zr(IV) solution individually, and the adsorption process was carried out under ideal circumstances (pH = 4 and ambient temperature). The samples were centrifuged, and then the adsorbed amount was calculated for each investigated metal ion. For desorption, the metal ion loaded was transferred into 0.05 L of 0.1M HCl and shaked for 2 h. Following that, distilled water was applied to wash the adsorbent until the pH was neutral. The adsorption capacity (q_e mg/g) for the metal ions under consideration was calculated at the completion of the five cycles.

Desorption efficiency percent (DE%) was calculated using the following equation:

DE % = Amount desorbed/Amount initially adsorbed X100

3. RESULT AND DISCUSSION

3.1 Characterization:

3.1.1 FTIR spectra:

The most noticeable chitosan peaks can be found in the FT-IR spectra at figure 1 from which it is clear that, at 3446 cm^{-1} (O H stretch), 2920 cm^{-1} (CH_2 asymmetric stretch), 2875 cm^{-1} (C H stretch), 1656 (amide band), 1599 cm^{-1} (NH_2 band), 1322 cm^{-1} (C N stretch), 1156 cm^{-1} (bridge O stretch), 896 cm^{-1} (pyranoid ring stretch), and 1086 cm^{-1} (C O stretch). In addition to the chitosan typical peaks, the spectra of three products also display some new absorption peaks. The recognizable poly (acrylic acid) peaks appear at 1717, 1683, 1576, 1456, and 621 cm^{-1}, whilst the COOH and COO− groups are denoted by the peaks at 1717 and 1683 cm^{-1}. It is easy to see the COOH group peak at 1722 cm^{-1}. Consequently, the polymer's acrylic acid was bonded to chitosan, and the structures of the three products should be quite similar [33–35].

3.1.2 Morphology

The pore size distribution (PSD) of pure chitosan (Fig. 2(b)) revealed a predominantly mesoporous structure with pore diameters about 20nm. The pores were irregularly distributed, reflecting the natural polymer's amorphous structure. The average pore diameter was approximately 80 nm.

Upon incorporation of poly(acrylic acid), the pore size distribution shifted significantly (Fig. 2(a)). This is attributed to the interpenetrating polymer network (IPN) formed between chitosan and PAA, which increases free volume and prevents dense packing of chitosan chains. The average pore diameter increased to 25nm. On other side, The SEM micrographs of pure chitosan revealed a relatively smooth and dense surface with limited porosity. Upon incorporation of poly(acrylic acid), a significant transformation in surface morphology was observed. The CS–PAA composite exhibited a **rougher, more heterogeneous surface** with a highly porous architecture. SEM images showed well-developed pores and interconnected channels, suggesting the formation of an interpenetrating polymer network (IPN).

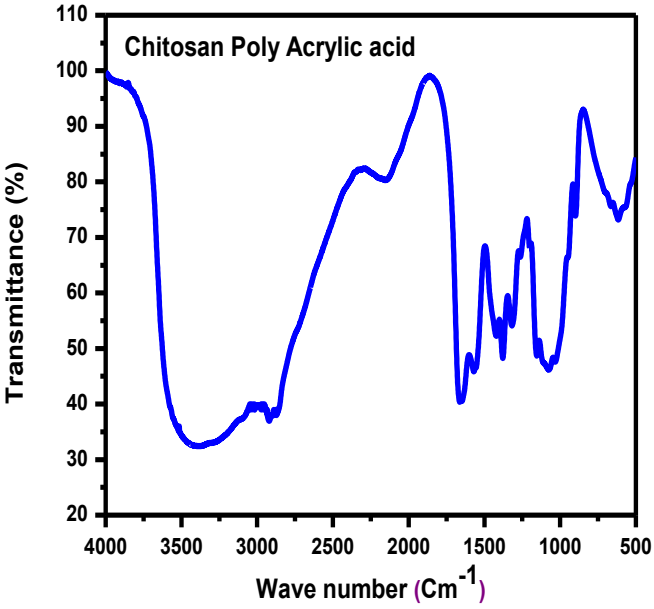

Fig. (1:) FT-IR for chitosan poly acrylic acid.

3.1.4 Chemical stability of the polymer.

A number of tests were conducted at pH range 1-12 to look into how pH levels affected the stability of the prepared CS–PAA polymer, through gravimetric analysis—monitoring the mass change of the complex after exposure to different pH environments over time. The weight loss % of the prepared CS-PAA at various pH is displayed in Figure 4 from which it is clear that, the polymer shows 38 weight loss % under strong acidic conditions at pH < 3.

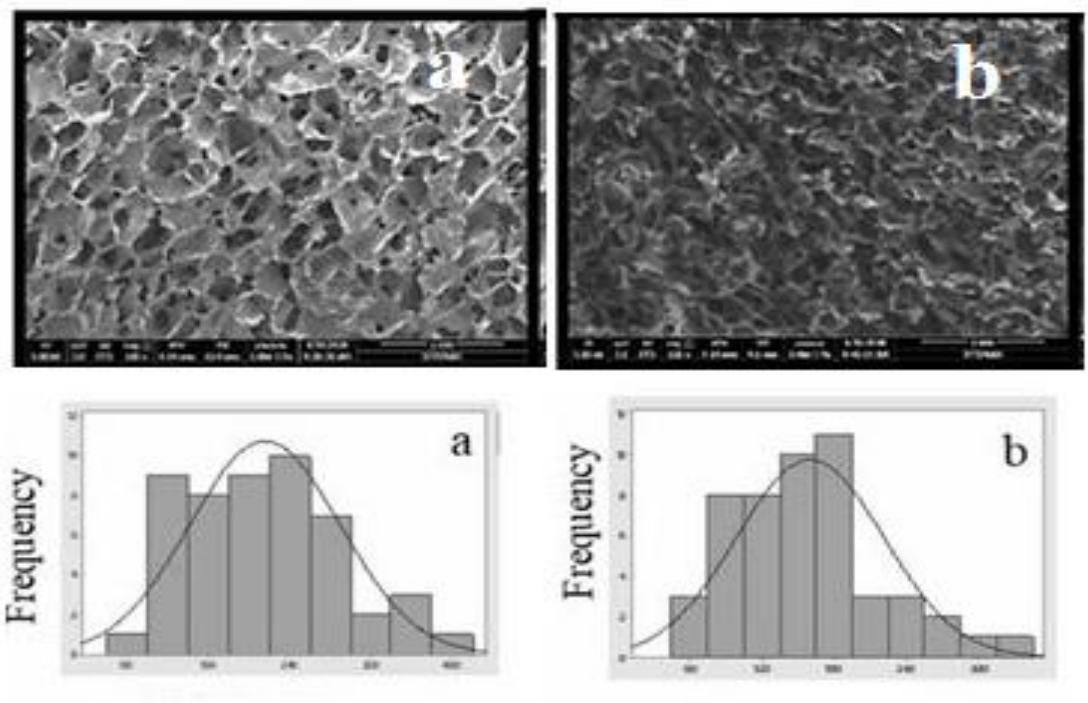

Fig. (2:) Scanning electro-microscope and the pore size distributions of a) chitosan poly acrylic acid b) chitosan.

3.1.3 Thermal analysis

Water content and its thermal sensitivities properties present in CS and CS-PAA are ascertained by thermal analysis (TGA). Figure 3. Three phases of weight loss are visible in TGA of chitosan polyacrylic acid. The first stage initiated at 30°C and continues until 110°C, during which time the weight decreased by 9% as a result of the loss of bound and adsorbed water. The breakdown of various groups and the breakdown of chitosan may be aided by the second stage at 320°C and the third step at 520°C. [36].

This may be due to the protonation of NH_3^+ group in chitosan. Results also demonstrated that the polymer is stable at acidic conditions with pH values between 4.0 and 7.0, as the weight loss % shows its minimum values 4%. This may be attributed to that, CS and PAA are partially ionized when the pH falls between 4.0 and 5.0. By means of ionic contact, the partially ionized CS and PAA can create a matrix of compact polyelectrolytes.

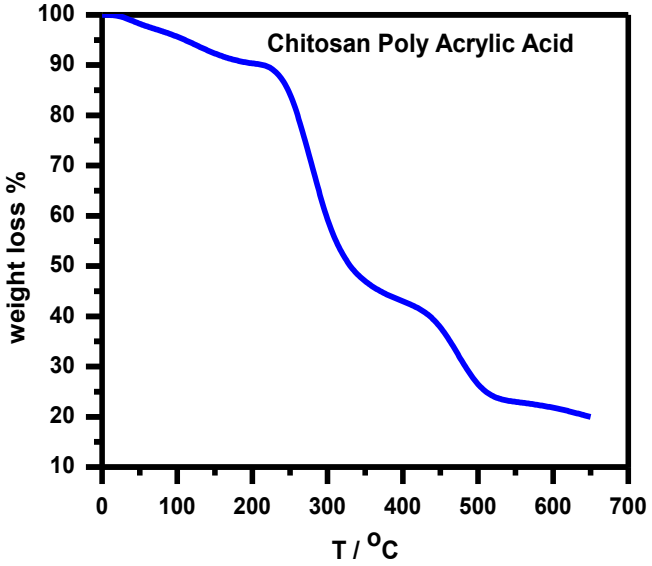

Fig. (3): Thermal analysis of chitosan and chitosan poly acrylic acid.

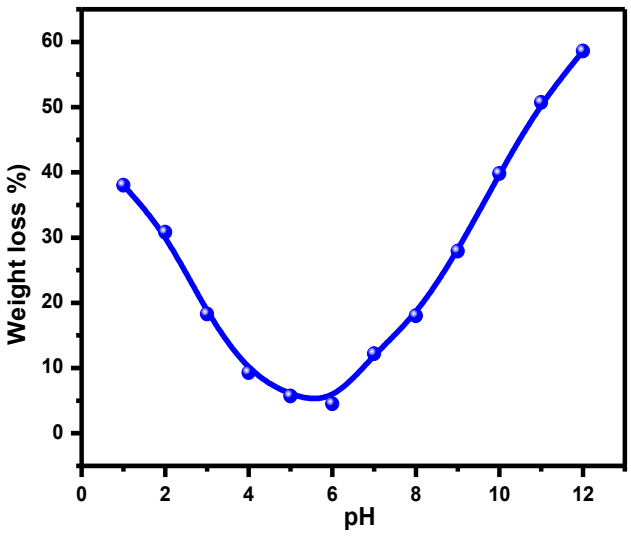

Fig. (4): Chemical stability of CS-PAA at different pH.

Moreover, in more acidic environments, such pH 4.0, the majority of PAA's carboxylic groups take the form of COOH. In the pH range of 4.0 to 5.0, CS and PAA exhibit partial dissociation. By ionic contact, the partially ionized CS and PAA can form a complex of compact polyelectrolytes; however, by raising the pH from 4.0 to 6.0, the degree of PAA ionization and the charge density of the PAA molecules rose dramatically. This is because the acid molecules may disrupt the interaction between NH_3^+ and COO^- in the CS–PAA particles, causing the chain stretch of CS and PAA. The maximum weight loss% was observed at pH range 9-12 it reaches 52% this may be attributed to the uncharged -NH2 with and ionized $-COO^-$. The chemical stability of CS-PAA can be summarized in Table 1.

3.2 Bach Investigation.

3.2.1 Acidic Medium effect on Adsorption capacity.

Figure 5 shows the impact of hydrochloric acid concentration, [HCl] on the capacity q_e of CS-PAA for Sr, Gd and Zr metal ions. It is clear that, generally the capacity lowers as acidity increases for all ions, this may be attributed to the Protonation of carboxyl and amino groups (reducing active sites) and the competitive adsorption between metal ions and excess H^+ ions. Zr (III) shows the least reduction in q_e with increasing acidity since 45 mg/g of its adsorption capacity still retain at 0.5 M HCl, indicating strong complexation ability and preference for oxygen donor ligands even in harsh acid conditions. Sr (II) is the most sensitive metal ion to acid concentration. The adsorption capacity drops by over 80 mg/g (from 36.7 to 8.2 mg/g), due to weak electrostatic interactions and inability to compete with protons. Highly acidic conditions, the carboxyl (–COOH) and amino ($–NH_2$) functional groups present in CS–PAA are predominantly protonated, reducing their ability to coordinate metal ions. However, despite this, metal ion uptake was still observed, with notable differences based on the valence state and ionic characteristics of each ion.

To elucidate the role of poly(acrylic acid) incorporation in enhancing adsorption performance, control experiments were conducted using pure chitosan hydrogel (CS) and chitosan–poly(acrylic acid) hydrogel (CS–PAA) prepared. The adsorption capacities for Sr(II), Gd(III), and Zr(IV) were determined under the same conditions pH 4, contact time 120 min, and adsorbent weight 0.2 g). Data obtained are illustrated at Table 2 from which it is clear that, across the three tested cations, CS–PAA exhibited markedly higher adsorption capacities compared to pure chitosan. The most significant relative enhancement was observed for Zr(IV), followed closely by Gd(III) and Sr(II). This performance trend can be attributed to both the stronger electrostatic interactions afforded by the additional –COOH groups from PAA and the increased surface functional group density in the composite hydrogel. Chitosan's adsorption is primarily driven by the chelation of metal ions via $–NH_2$ groups (protonated under acidic to neutral conditions) and surface hydroxyl groups. While effective, its capacity is limited by the relatively low density of binding sites and partial solubility constraints under acidic conditions.

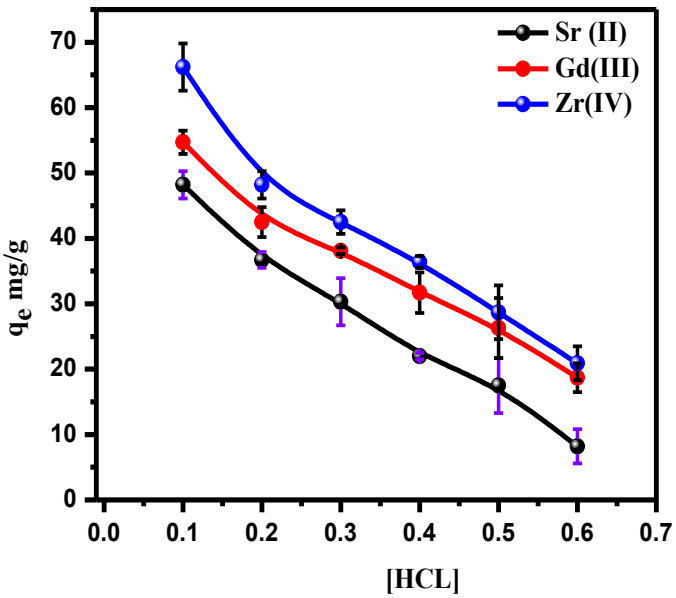

Fig. (5): Adsorption Capacity, q_e of CS–PAA for Sr^{2+}, Gd^{3+}, and Zr^{4+} at Different HCl Concentrations.

Table (1): Chemical stability of CS-PAA at different pH

pH Range	Weight Loss (%)	Interaction Type	Chemical Behavior	Stability Description
1-3	38	Chitosan fully protonated **($–NH_3^+$).** PAA mostly –COOH (non-ionized)	Chitosan: protonated PAA: largely uncharged	Weak interaction due to limited ionization of PAA. Complex may swell or partially dissolve. Stability is low to moderate.
4-6	4	Chitosan still protonated PAA starts deprotonating **($–COO^-$)**	Chitosan: protonated PAA: deprotonated	Ideal pH for maximum electrostatic interaction → Strong complex formation and high stability. Minimal degradation.
7-8	18	Chitosan begins to lose protonation. PAA fully ionized **($–COO^-$)**	Chitosan: starts deprotonating PAA: fully deprotonated	Electrostatic attraction weakens. Stability decreases. Complex may start disassembling or swell significantly.
9-12	52	Chitosan is mostly uncharged **($–NH_2$).** PAA remains ionized **($–COO^-$)**	Chitosan: uncharged PAA: fully deprotonated	Minimal electrostatic interaction. Complex is unstable. Likely to dissociate **or** dissolve, especially under alkaline conditions.

Table (2): The equilibrium adsorption capacities (q_e, $mg \cdot g^{-1}$) and removal efficiencies (%R) for both hydrogels.

Metal ion	CS (q_e mg/g)	CS PAA (q_e mg/g)
Sr(II)	22.6	48.2
Gd(III)	30.4	54.7
Zr(IV)	38.3	66.2

3.2.2 Effect of Time

As shown in Figure 6, The impact of time duration on uptake % of Sr(II), Gd(III), and Zr(IV) ions onto the CS–PAA hydrogel were examined during a period of 5 to 120 minutes pH = 4 and room temperature. For all three metal ions, the data show a time-dependent raise the uptake %, with a steep increase in the early phases and a plateau at longer contact durations. All species had comparatively low uptake % at 5 minutes, reaching 8.7 %, 15.42 %, and 24.2 %, for Sr(II), Gd(III), and Zr(IV) respectively. There was a noticeable increase in adsorption as contact duration increased. After 30 minutes, the uptake % had increased to 52.8 %, 71.96 %, and 84.5 %, for Sr(II), Gd(III), and Zr(IV) respectively. After around 60 minutes, equilibrium was reached, and only slight increases in uptake % were seen. It was 92.2 % for Zr(IV), 82.9 % for Gd(III), and 62.8 % for Sr(II). According to this saturation tendency, the CS–PAA surface's accessible active sites gradually fill up with time, becoming scarcer after 60 minutes. The strong concentration gradient between the solution and adsorbent, additionally, a significant quantity of active binding sites on the CS–PAA surface, are responsible for the initial rapid absorption. Equilibrium is reached due to the gradual migration of examined ions into the inner pores and the repulsive forces between incoming and already deposited metal ions. Zr(IV) had the greatest uptake % over the whole time range among the three metal ions, followed by Gd(III) and Zr(IV). Variations in ionic size, charge density, and binding affinity for the functional groups (-COOH and $-NH_2$) of the CS–PAA matrix could account for this tendency. Zr(IV) has a greater valence state, but slower diffusion kinetics or steric hindrance may be the cause of its decreased absorption.

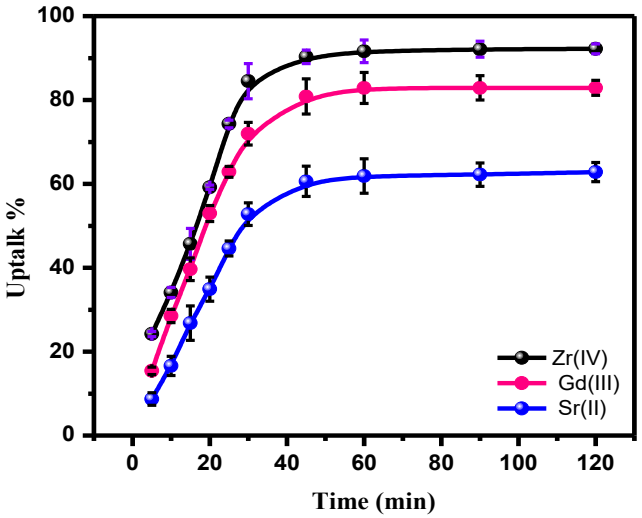

Fig. (6): Effect of contact time on the adsorption of Sr(II), Gd(III), and Zr(IV) on CS-PAA at pH=4, C_o=50 mg/g and 25ºC.

3.2.3 Kinetic Adsorption

Adsorption rat of investigated ions onto the chitosan–poly(acrylic acid) hydrogel were investigated through pseudo second order, Elovich and Intraparticle diffusion (IPD) models to elucidate the underlying sorption technique. Models are fitted and represented at Figure 7 which declare that, Pseudo and Elovich fitted well than Intra particle diffusion model. The obtained data are represented in Table 3 which makes it evident that, the kinetic data exhibited excellent agreement with the pseudo model, as indicated by high correlation coefficients (R^2 = 0.99 for Zr(IV), 0.98 for Gd(III), and 0.97 for Sr(II)). Table 3 shows that, the calculated equilibrium adsorption capacities (qe) were 78.9 mg/g for Zr(IV), 32.3 mg/g for both Gd(III) and Sr(II), closely matching experimental values. The high values of the rate constant K_2 (0.0482, 0.0467, and 0.0572 g/mg·min for Zr, Gd, and Sr, respectively) confirm a chemisorption-driven mechanism, likely involving complexation between the investigated ions and the functional groups (–COOH, $–NH_2$, –OH) present in the CS–PAA matrix. The superior sorption capacity for Zr(IV) may be attributed to its higher charge density and stronger interaction with the sorbent. Moreover, the Elovich model also provided an excellent fit to the data from experiments, with R^2 values of 0.95 for Zr(IV) and Gd(III), and 0.94 for Sr(II), supporting the involvement of heterogeneous chemisorption. The initial adsorption rate (α) was highest for Zr(IV) (10.3 mg/g·min), then Gd(III) (8.7 mg/g·min) and Sr(II) (6.3 mg/g·min), correlating with their respective β values and affinity toward the sorbent surface. The higher α value for Zr(IV) further indicates a more rapid and favorable adsorption process in the early stages of contact time, consistent with strong surface interaction and complexation behavior. With R^2 values ranging from 0.89 to 0.92, the IPD model showed a respectably high degree of fit, suggesting that while intra-particle diffusion plays a role in the adsorption process, it is not the only rate-limiting phase. The boundary layer thickness, inferred from the intercept (θ), was highest for Zr(IV) (θ = 18.5 mg/g), suggesting a greater influence of surface adsorption prior to diffusion into interior pores. Gd(III) and Sr(II) showed lower θ values (16.7 and 12.9 mg/g, respectively), reflecting a relatively more significant contribution from internal pore diffusion[37].

3.2.4 Isotherm adsorption

Four isotherm models were used to assess equilibrium data for the purpose of better comprehend the adsorption mechanism of Sr(II), Gd(III), and Zr(IV) ions onto chitosan–poly(acrylic acid) (CS–PAA) hydrogel: Langmuir, Freundlich, Temkin, and Sips [39-41]. Figure 8 displays the four models' fittings, demonstrating how well-suited each model is. A uniform surface with limited, equal binding sites is assumed by the Langmuir model based on the data calculated and displayed in Table 4. R^2 = 0.94 for Sr(II) illustrates that the model matches the experimental data rather well, whereas R^2 > 0.97 for Gd(III) and Zr(IV) shows that the model fits the data better. Their decreasing hydrated radius and increasing ionic charge matched the maximal adsorption capabilities (q_{max}), which exhibited the following pattern: Zr > Gd > Sr. These findings suggest that monolayer formation at higher energy regions is favored by the adsorption of multivalent cations. Furthermore, excellent adsorption was demonstrated at all concentrations by the separation factor (R_L) values, which varied from 0 to 1. On other side, Sr in particular (R2 = 0.96) fits the Freundlich model, which predicts adsorption on heterogeneous surfaces, quite well. The heterogeneity factor (1/n) value for each ion was less than 1, suggesting nonlinear and beneficial adsorption. Higher affinity for active sites and stronger adsorption intensities were indicated by Gd and Zr's 1/n values being closer to 0.4. This result supports the existence of energetically diverse functional groups on the hydrogel, including -OH, -NH2, and -COOH. The Temkin model accounts for indirect interactions between adsorbed ions and assumes a linear decrease in adsorption energy. It was evident that electrostatic interactions dominated adsorption (chemisorption) since the heat of adsorption (b_T) measurements were within the range expected for physisorption (< 40 kJ/mol). Gd and Zr displayed higher K_T values, indicating stronger interactions, due to their bigger charge densities and stronger complexation with the hydrogel matrix. The Sips model, which combines the Freundlich and Langmuir isotherms, provided the most appropriate fit for all three ions (R^2 > 0.98), accurately describing adsorption over the entire concentration range. The ns values for Gd and Zr approached 1, indicating Langmuir-like behavior at higher concentrations, whereas ns < 1 for Sr confirmed surface heterogeneity and a less specific interaction. The Sips model projected that Zr would have the highest maximum adsorption capability (q_s) at ~70.6 mg/g, then Gd (~62.7 mg/g) and Sr (~51.6 mg/g).

Table (3): Kinetic parameters for the adsorption of Zr(IV), Gd(III), and Sr(II) on CS-PAA

Metal ions	*Pseudo second order*			*Elovich*			*Intra particle diffusion*		
	q_e mgg^{-1}	K_2 gmg^{-1} min^{-1}	R^2	B gmg^{-1}	α mgg^{-1} $min^{-1/2}$	R^2	θ mgg^{-1}	K_1 min^{-1}	R^2
Zr(IV)	78.9	0.0482	0.99	0.307	10.3	0.95	18.5	8.2	0.92
Gd(III)	32.3	0.0467	0.98	0.423	8.7	0.95	16.7	6.8	0.91
Sr(II)	32.3	0.0572	0.97	0.576	6.3	0.94	12.9	6.2	0.89

Table (4): Isotherm model parameters for adsorption os Sr(II), Gd(III) and Zr(IV) on to CS-PAA hydrogel.

Isotherm models	Parameters	Sr(II)	Gd(III)	Zr(IV)
Experimental data	q_{exp} (mg/g)	48.2	57.6	66.7
Langmuir	q_{max} (mg/g)	68.9	74.2	80.4
	K_L (L/mg)	0.032	0.052	0.069
	R^2	0.941	0.969	0.979
Freundlich	K_F (mg/g)(L/mg)$^{1/n}$	12.1	18.8	23.1
	1/n	0.64	0.49	0.43
	R^2	0.962	0.975	0.977
Temkin	b_T (J/mol)	32.8	33.3	34.1
	K_T (L/g)	0.83	1.22	1.48
	R^2	0.927	0.953	0.965
Sips	q_s (mg/g)	51.6	62.7	70.4
	K_s (L/mg)	0.025	0.047	0.063
	Ns	0.79	0.93	0.98
	R^2	0.982	0.991	0.994

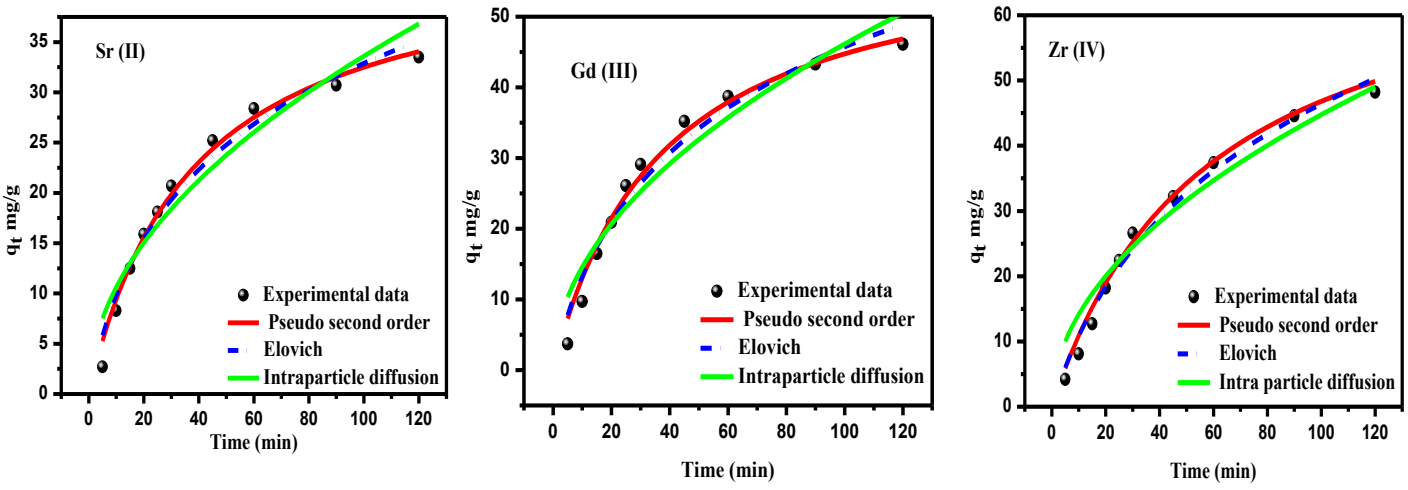

Fig (7): Kinetic adsorption models for Sr(II), Gd(III), and Zr(IV) on CS-PAA.

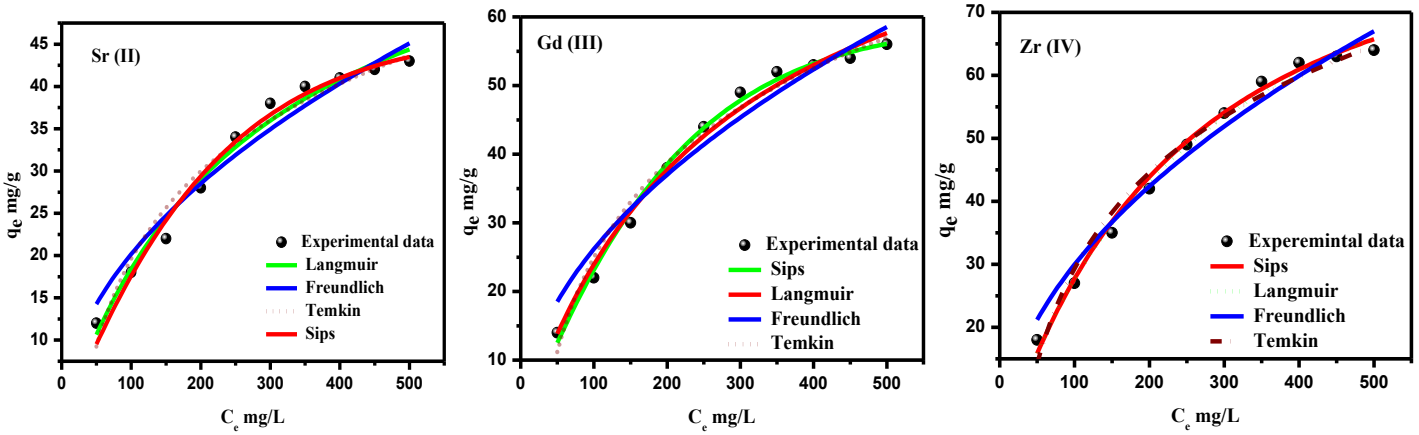

Fig. (8): Isotherm adsorption models for Sr(II), Gd(III), and Zr(IV) on CS-PAA.

3.2.5 Adsorption–Desorption Cycles for Sr^{2+}, Gd^{3+}, and Zr^{4+}

0.1 M HCl is applied to evaluate the regeneration behavior of the chitosan–poly(acrylic acid) (CS–PAA) adsorbent toward Gd^{3+}, Zr^{4+}, and Sr^{2+} was objectively assessed throughout five cyclic adsorption-desorption, as shown within Figure 9. The outcomes showed the material's strong reusability and effective capability for ion recovery. Among the tested ions, Zr^{4+} showed that the first maximum adsorption capacity is (65.8 mg/g), then Gd^{3+} (52.4 mg/g) and Sr^{2+} (48.5 mg/g). The superior performance for Zr^{4+} can be attributed to its higher valence and strong electrostatic interaction with the carboxylic and hydroxyl functional groups present in the CS–PAA matrix. Gd^{3+}, with its trivalent nature and moderate ionic radius, also formed stable complexes with the polymeric matrix, while Sr^{2+}, being divalent and less electropositive, exhibited a comparatively lower affinity. Throughout the five regeneration cycles, the Desorption efficiencies remained high, exceeding 85% for all ions, indicating effective regeneration with mild acid treatment and minimal irreversible binding. The adsorption capacity gradually decreased by about 15–20%, reflecting a slight reduction in active sites or incomplete desorption with repeated use. Such outcomes illustrate that, the CS–PAA hydrogel is a durable and effective adsorbent for multivalent metal ions. The material showed preferential adsorption toward higher-valence ions (Zr^{4+} > Gd^{3+} > Sr^{2+}), which is advantageous in selective separation and recovery processes, particularly in nuclear waste treatment or rare earth purification applications [42-43].

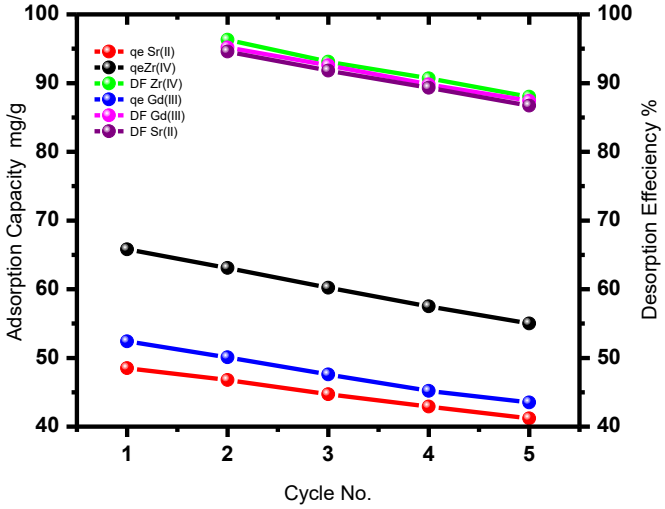

Fig. (9): Adsorption–Desorption Performance of CS–PAA for Sr(II), Gd(III), and Zr(IV) over Five Cycles at pH=4, C_o=100 mg/g and 25°C.

CONCLUSION

CS–PAA hydrogel was produced and its structural characteristics were verified by TGA, SEM, and FTIR studies. The FTIR spectrum showed the characteristic bands of functional groups of the produced hydrogel and the interaction between $–NH_2$ and –COOH groups, thus the formation of a polyelectrolyte complex was well established. SEM microphotographs showed a very rough, porous, and interconnected surface morphology which is characteristic of a developed interpenetrating polymer network, convenient for adsorption and diffusion phenomena. Elemental analysis Chemical compositions of the pure chitosan and CS–PAA composite were evaluated using EDX. The chemical stability of CS-PAA hydrogels across a pH range of 1–12 is governed by the ionization behavior of the two polymers and the intermolecular interactions between

them. Kinetic models declare that, the adsorption process of Zr(IV), Gd(III), and Sr(II) onto CS–PAA is governed primarily by chemisorption, with additional contributions from intra-particle diffusion and surface heterogeneity. The chitosan–poly(acrylic acid) hydrogel exhibits strong adsorption capacity toward multivalent metal ions, with performance increasing in the order Sr(II) < Gd(III) < Zr(IV). The Sips model best describes the adsorption behavior, indicating a combination of monolayer coverage and surface heterogeneity. These findings highlight the hydrogel's potential in water purification, particularly in treating radioactive and industrial wastewater.

REFERENCES

[1] G.R Mahdavinia a, A Pourjavadi a, H Hosseinzadeh a, M.J Zohuriaan Modified chitosan 4. Superabsorbent hydrogels from poly(acrylic acid-co-acrylamide) grafted chitosan with salt- and pH-responsiveness properties, Eur. Polym., 40 (7), 2004, 1399-1407.

[2] Sofien Benltoufa a b, Wafa Miled c d, Mariem Trad a b, Rihab Ben Slama e, Faten Fayala Chitosan hydrogel-coated cellulosic fabric for medical end-use: antibacterial properties, basic mechanical and comfort properties, Carbohyd Polym, 227(1), 2020, 115352.

[3] Qiu H, Yu J, Zhu J. Polyacrylate/(Chitosan Modified Montmorillonite) Nanocomposite: Water Absorption and Photostability. Polym Polym Compos. 13, 2005, 167–72.

[4] Madian NG, El-Hossainy M, Khalil WA. Improvement of the physical properties of chitosan by γ-ray degradation for wound healing. Results Phys. 11, 2018, 951–5

[5] Jeung S, Mishra MK. Hot melt reactive extrusion of chitosan with poly(acrylic acid). Int J Polym Mater Polym Biomater. 60, 2011, 102–13.

[6] Ghazy OA, Khalil SA, Senna MM. Synthesis of montmorillonite/chitosan/ammonium acrylate composite and its potential application in river water flocculation. Int J Biol Macromol. 163, 2020, 1529–37.

[7] Ghazy O, Hamed MG, Breky M, Borai EH. Synthesis of magnetic nanoparticles-containing nanocomposite hydrogel and its potential application for simulated radioactive wastewater treatment. Colloids Surfaces A Physicochem Eng Asp., 621, 2021, 126613.

[8] Grande-Tovar CD, Vallejo W, Zuluaga F. Equilibrium and kinetic study of lead and copper ion adsorption on chitosangrafted-polyacrylic acid synthesized by surface initiated atomic transfer polymerization. Molecules., 23, 2018, 2218.

[9] Alhassanieh, O., Ajji, Z., Alkourdi, H., and Haloum, D., Migration of strontium, cesium, and europium from poly (butyl acrylate)/phosphate/composites prepared using gamma radiation. *Applied Radiation and Isotopes*, 69(2), 2011, 448–454.

[10] Arifi, A. and Hanafi, H., Adsorption of cesium, thallium, strontium and cobalt radionuclides using activated carbon. *Asian Journal of Chemistry*, 23(1), 2011, 111.

[11] Bhattacharya, A., Naiya, T., Mandal, S., and Das, S. (2008). Adsorption, kinetics and equilibrium studies on removal of Cr (vi) from aqueous solutions using different low-cost adsorbents. *Chemical engineering journal*, 137(3), 2008, 529–541.

[12] Celebi, O., Kilikli, A., and Erten, H., Sorption of radioactive cesium and barium ions onto solid humic acid. *Journal of hazardous materials*, 168(2), 2009, 695–703.

[13] EI-Naggar, I., Mowafy, E., Abdel-Galil, E., and Ghonaim, A. K., Adsorption of some hazardous radionuclides from their aqueous waste solutions using synthetic silico (iv) titanate. *Arab Journal of Nuclear Sciences and Applications*, 41(3), 2008, 2–14.

[14] Faghihian, H., Moayed, M., Firooz, A., and Iravani, M., Evaluation of a new magnetic zeolite composite for removal of Cs^+ and Sr^{2+} from aqueous solutions: Kinetic, equilibrium and thermodynamic studies. *Comptes Rendus Chimie*, 17(2), 2004, 108 – 117.

[15] Gupta, V. K., Jain, R., Mittal, A., Saleh, T. A., Nayak, A., Agarwal, S., and Sikarwar, S., Photo-catalytic degradation of toxic dye amaranth on tio 2/uv in aqueous suspensions. *Materials Science and Engineering: C*, 32(1), 2012, 12–17.

[16] Lahiri, S., Roy, K., Bhattacharya, S., Maji, S., and Basu, S., Separation of 134 cs and 152 eu using inorganic ion exchangers, zirconium vanadate and ceric vanadate. *Applied radiation and isotopes*, 63(3), 2005, 293– 297.

[17] Lewis, F. W., Hudson, M. J., and Harwood, L. M. (2011). Development of highly selective ligands for separations of actinides from lanthanides in the nuclear fuel cycle. *Synlett*, 18, 2011, 2609–2632.

[18] Long, H., Wu, P., and Zhu, N., Evaluation of Cs^+ removal from aqueous solution by adsorption on ethylamine-modified montmorillonite. *Chemical engineering journal*, 225, 2013, 237–244.

[19] Luo, X., Wang, C., Luo, S., Dong, R., Tu, X., and Zeng, G., Adsorption of as (iii) and as (v) from water using magnetite Fe_3O_4-reduced graphite oxide-MnO_2 nanocomposites. *Chemical Engineering Journal*, 187, 2012, 45–52.

[20] Mertz, J. L., Fard, Z. H., Malliakas, C. D., Manos, M. J., and Kanatzidis, M. G. (2013). Selective removal of cs+, sr2+, and ni2+ by k2 x mg x sn3–x s6 (x= 0.5–1)(kms-2) relevant to nuclear waste remediation. *Chemistry of Materials*, 25(10):2116–2127.

[21] Metwally, S., El-Gammal, B., Aly, H., and Abo-El-Enein, S. (2011). Removal and separation of some radionuclides by poly-acrylamide based ce (iv) phosphate from radioactive waste solutions. *Separation Science and Technology*, 46(11):1808–1821.

[22] Moloukhia, H., Hegazy, W., Abdel-Galil, E., and Mahrous, S. (2014). Removal of eu^{3+}, ce^{3+} ,sr^{2+} and cs^+ ions form radioactive waste solutions by modified activated carbon prpared from coconut shells. *Chemsitry and Ecology*.

[23] Ossman, M., Mansour, M., Fattah, M., Taha, N., and Kiros, Y. (2014). Peanut shells and talc powder for removal of hexavalent chromium from aqueous solutions. *Bulgarian Chemical Communications*, 3(3):629–639.

[24] Sachse, A., Merceille, A., Barr´e, Y., Grandjean, A., Fajula, F., and Galarneau, A. (2012). Macroporous lta-monoliths for in-flow removal of radioactive strontium from aqueous effluents: application to the case of fukushima. *Microporous and Mesoporous Materials*, 164:251–258.

[25] Sahu, M. K., Mandal, S., Yadav, L. S., Dash, S. S., and Patel, R. K. (2016). Equilibrium and kinetic studies of cd (ii) ion adsorption from aqueous solution by activated red mud. *Desalination and Water Treatment*, 57(30):14251–14265.

[26] Saleem, M., Afzal, M., and Hanif, J. (1993). Selective adsorption of cerium on activated charcoal from aqeous electrolyte solutions. *J. Radioanal Nucl Chem*.

[27] Tang, B., Fang, Y., Zhang, S., Ning, H., and Jing, C. (2011). Preparation and characterization of cordierite powders by water-based sol-gel method.

[28] Singh, V., Sharma, A.K., Tripathi, D.N., Sanghi, R., (2009). Poly(methylmethacrylate) grafted chitosan: An efficient adsorbent for anionic azo dyes. J. Hazard. Mater. 161, 955–966.

[29] Carlos Mongay, Victor Cerda, A Britton-Robinson buffer of known ionic strength, J. of Annali Chemica, 64, 1974, 409-412.

[30] Ho, Y.-S., McKay, G.J.P. (1999) biochemistry, Pseudo-second order model for sorption processes. Process Biochem. 34, 451–465.

[31] Langmuir I, (1918) The adsorption of gases on plane surfaces of glass, mica and platinum. J Am Chem Soc 40, 1361–1403.

[32] Freundlich H, Adsorption in solution. Phys Chem Soc 40 (1906) 1361–1368.

[33] Mulan Zhu , Benqiao He , Wenying Shi , Yaohui Feng , Jincheng Ding , Jianxin Li, Fandi Zeng, (2010), Preparation and characterization of PSSA/PVA catalytic membrane for biodiesel production. J. Fuel 89, 299-304.

[34] Ismail AF, Zubir N, Nasef MM, Dahlan KM, Hassan AR. (2005) Physico-chemical study of sulfonated polystyrene pore-filled electrolyte membranes by electrons induced grafting. J Membr Sci 254, 189-196.

[35] Shang X, Tian S, Kong L, Meng Y. (2005), Synthesis and characterization of sulfonated fluorene-containing poly(arylene ether ketone) for proton exchange membrane. J Membr Sci, 266, 94-101.

[36] Huacai Ge∗, Senkang Wang, (2014) Thermal preparation of chitosan–acrylic acid superabsorbent: Optimization, characteristic and water absorbency J. Carbohydrate Polymers 113, 296-303.

[37] Ghazy O, Hamed MG, Breky M, Borai EH. (2021) Synthesis of magnetic nanoparticles-containing nanocomposite hydrogel and its potential application for simulated radioactive wastewater treatment. Colloids Surfaces A Physicochem Eng Asp. 621:126613.

[38] Müller A, Österlund H, Marsalek J, Viklander M. (2020) The pollution conveyed by urban runoff: A review of sources. Vol. 709, Science of the Total Environment. Elsevier B.V.; 136125.

[39] Vardhan KH, Kumar PS, Panda RC. (2019), A review on heavy metal pollution, toxicity and remedial measures: Current trends and future perspectives. Journal of Molecular Liquids. Elsevier B.V.; 290: 111197.

[40] El-Safy S, Tammam SN, Abdel-Halim M, Ali ME, Youshia J, Shetab Boushehri MA, (2020). Collagenase loaded chitosan nanoparticles for digestion of the collagenous scar in liver fibrosis: The effect of chitosan intrinsic collagen binding on the success of targeting. Eur J Pharm Biopharm. ; 148:54–66.

[41] Moreno-Sader K, Meramo-Hurtado SI, González-Delgado AD. (2020), Environmental sustainability analysis of chitosan microbeads production for pharmaceutical applications via computer-aided simulation, WAR and TRACI assessments. Sustain Chem Pharm. 2020; 15:100212.

[42] Saeed RM, Dmour I, Taha MO. (2020), Stable Chitosan-Based Nanoparticles Using Polyphosphoric Acid or Hexametaphosphate for Tandem Ionotropic/Covalent Crosslinking and Subsequent Investigation as Novel Vehicles for Drug Delivery. Front Bioeng Biotechnol. 24; 8:4.

[43] Ghazy OA, Khalil SA, Senna MM. (2020),Synthesis of montmorillonite/chitosan/ammonium acrylate composite and its potential application in river water flocculation. Int J Biol Macromol. 163:1529–37.